




Does the non-force-freeness matter for the extrapolation of solar magnetic field?

FU YU ^{1,2,3} JIE ZHAO ^{1,3} YANG SU ^{1,2} XIAOSHUAI ZHU ³ AND YANG GUO ⁴

¹Key Laboratory of Dark Matter and Space Astronomy, Purple Mountain Observatory, Chinese Academy of Sciences, Nanjing 210023, People's Republic of China

²School of Astronomy and Space Science, University of Science and Technology of China, Hefei 230026, People's Republic of China

³State Key Laboratory of Space Weather, National Space Science Center, Chinese Academy of Sciences, Beijing, 100190, People's Republic of China

⁴School of Astronomy and Space Science and Key Laboratory for Modern Astronomy and Astrophysics, Nanjing University, Nanjing 210023, People's Republic of China

(Accepted on 25-Oct-2022 by APJ)

ABSTRACT

Magnetic field extrapolation is a fundamental tool to reconstruct the three-dimensional solar coronal magnetic field. However, the prevalently used force-free field model might not be applicable in the lower atmosphere, where plasma β is greater than 1. In this work, we perform extrapolation in active region 12158, based on an updated magnetohydrostatic (MHS) method. By comparing the results with those from the force-free field method of Current-Field Iteration in Spherical Coordinates (CFITS), we find that the overall properties, which are characterized by the magnetic free energy and helicity, are roughly the same after volume integral. The major differences lie in the magnetic configuration and the twist number of magnetic flux rope (MFR). A coherent MFR with twist around 1 is reproduced from CFITS. In another manner, two sets of MFR, which are highly twisted and slightly coupled, are derived by the MHS method. The latter one is better constrained by the high-resolution observations, such as the filament fibrils, pre-eruptive braiding characteristics and the eruptive double-J shaped hot channel. Overall, our work shows the MHS method is more promising to reproduce the magnetic fine structures that can well match the observations not only in the chromosphere but also in the corona. This initiates the necessity of reconsidering the simplification of low atmosphere for currently widely used nonlinear force-free extrapolation method, since such assumption will not only omit the magnetic structures at low atmosphere but also affect those obtained in the corona, and therefore bringing in ambiguity in interpreting the solar eruption.

Keywords: Solar photosphere (1518); Solar chromosphere (1479); Solar corona (1483); Solar extreme ultraviolet emission (1493); Solar active regions (1974); Solar magnetic fields (1503)

1. INTRODUCTION

Solar eruptions, especially those from active regions (ARs), are acknowledged to be the major driving sources of catastrophic space weather. The accompanying coronal mass ejections (CMEs) have become an important target for space weather monitored in remote observations and in in-situ measurements (Zhang et al. 2021). It is generally believed that the physical essence of CMEs is

the eruption of magnetic flux ropes (MFRs; Chen 1996; Titov & Démoulin 1999) that carrying plasma (Chen 2011). Therefore, studying the structure and evolution of MFRs is crucial to understand the physical mechanisms of CMEs and predict space weather. As it is currently difficult to measure the three-dimensional (3D) coronal magnetic field directly from observations, an alternative way of modeling coronal field with lower-layer magnetic field as bottom boundary is frequently used with the photospheric field (Sakurai 1989; Solanki et al. 2006; Wiegelmann et al. 2017; Wiegelmann & Sakurai 2021; Zhu et al. 2022) or the rarely obtained chromo-

spheric field (Wiegelmann et al. 2008; Harvey 2012; Jin et al. 2013; Lagg et al. 2017).

Overall, magnetohydrodynamics (MHD) approximation can provide a basic framework to outline the interaction between plasma and magnetic field in the solar atmosphere (Priest 2014). It is simplified under various conditions according to the two critical parameters of plasma β and Alfvén Mach number (Gary 2001; Wiegelmann et al. 2017). Plasma β evaluates the dominance of the plasma gas pressure over the magnetic pressure, while the Alfvén Mach number estimates the flow speed over the Alfvén speed. Generally, MHD approximation should be adopted for the outer corona where the plasma flow and plasma gas pressure dominate. In regions with low Alfvén Mach number and finite β , e.g., in the upper photosphere and chromosphere, a steady-state derives the magnetohydrostatic (MHS) model with the Lorentz force being balanced by the plasma pressure gradient and gravitational forces (Wiegelmann et al. 2017). Under a further simplified condition of low Alfvén Mach number and low plasma β , e.g., in the inner corona, the Lorentz force vanishes and the magnetic field becomes force-free, which is a state that assuming the dominance of the magnetic field over plasma. Models including nonlinear force-free field (NLFFF), linear force-free field (LFFF) and potential field are often applied to different force-free states (or current distributions) in terms of the force-free parameter (noted as α ; Wiegelmann 2008; Wiegelmann & Sakurai 2021). In particular, NLFFF extrapolations are favored for its relatively robust reconstructions and affordable computational resources in most cases. Various numerical methods have been developed to construct the NLFFF models, e.g., the optimization approach (Wheatland et al. 2000; Wiegelmann 2004), magneto-frictional method (Valori et al. 2007; Guo et al. 2016), MHD relaxation method (Jiang & Feng 2012), Grad-Rubin method (Amari et al. 2006; Gilchrist & Wheatland 2014) and flux rope insertion method (van Ballegoijen 2004; Su 2019).

Based on the force-free field methods, investigations have been carried out for understanding the initiation mechanism and the process of energy release during solar eruptions. Most of the works obtain an eruptive MFR with twist number around 1, and/or with decay index above the eruptive flux rope around $0.5 \sim 2$ (Sun et al. 2022) or $0.8 \sim 1.5$ (Zhong et al. 2021), which are consistent with the predictions of the kink instability and/or the torus instability. Some works however find eruptive MFR with a relatively high twist number (Guo et al. 2021) and such highly twisted structure is considered to be responsible for the interplanetary magnetic clouds (MCs) that are found to have a wide range

of twist number as high as 14.6 turns per astronomical unit from in-situ observations (Hu et al. 2014). The discrepancy of the obtained twist number from different extrapolation methods may lie in the force-free assumption that has been adopted for the entire atmosphere throughout the active region. By the MHD relaxation method, Zhu et al. (2016) found that the non-force-free region can reach height of $1.4 \sim 1.8$ Mm above the photosphere and non-force-freeness in the chromosphere has also been revealed by Leenaarts et al. (2015) in radiative MHD simulation. Moreover, necessities of including the non-force-freeness are already shown in Zhao et al. (2017) and Zhu et al. (2016) for investigating the magnetic structures of chromospheric features such as brightenings and fibrils.

For attaining a reliable picture of the solar eruption, it is essential to study the magnetic configuration under non-force-free assumption that matches better with the physical situation, especially in the lower atmosphere. Zhu & Wiegelmann (2018) developed an MHS extrapolation method for computing such magnetic configurations by taking into account plasma pressure and gravity. Based on the radiative MHD simulation (Cheung et al. 2019), comparison was carried out for the MHS and the NLFFF extrapolation (Zhu & Wiegelmann 2019). It is found that MHS method has more advantages in reconstructing long twisted magnetic field lines and in recovering the primary plasma structure in the lower atmosphere. With observation of vector magnetogram from Imaging Magnetograph eXperiment (IMaX, Martínez Pillet et al. 2011) on board SUNRISE (Barthol et al. 2011; Solanki et al. 2017), the extrapolations based on MHS and NLFFF are also compared and the results show that the two methods derive roughly similar magnetic structures, with the chromosphere magnetic field obtained by MHS method is more consistent with the chromosphere fibrils in direction (Zhu et al. 2020b). Moreover, Vissers et al. (2022) investigated the similarity between the chromospheric magnetic fields inferred from direct inversion and the MHS extrapolation. They found both methods provide a qualitatively similar chromospheric field. Although individual cases have shown the privilege of MHS method, the advantage is usually found below the chromosphere. To what extent shall we concern about the non-force-freeness when obtaining the corona magnetic field is still unclear and desires further investigation.

In this paper, we aim to explore the difference between the force-free and the non-force-freeness assumptions in reconstructing 3D magnetic field of active region. For this intention, AR 12158 which has been extensively studied (Cheng et al. 2015; Zhao et al. 2016; Zhou et al.

2016; Vemareddy et al. 2016; Duan et al. 2017; Lee & Magara 2018; Kilpua et al. 2021; Shen et al. 2022) is selected and carry out the extrapolation with newly updated MHS method (Zhu & Wiegelmann 2022). The results are compared with the ones from NLFFF extrapolation in Zhao et al. (2016) and other works. The paper is organized as follows: the observation characteristics are shown in Section 2.1 and the extrapolation methods, i.e., MHS and CFITS are introduced briefly in Section 2.2 and 2.3. The results are displayed in Section 3 and we present the summary and discussions in Section 4.

2. OBSERVATIONS AND EXTRAPOLATION METHODS

2.1. Observations

NOAA AR 12158, which is selected for this case study, is observed near the disk center (N15E03 in heliographic coordinates) on 2014 September 10 by the Solar Dynamics Observatory (SDO; Pesnell et al. 2012). During its passage through the solar disk, an X1.6 class flare happens at 17:21 UT according to the soft X-ray 1–8 Å flux from the Geostationary Operational Environmental Satellites (GOES), and a halo coronal mass ejection (CME) event is subsequently accompanied (see CME catalog¹ (Gopalswamy et al. 2009) from Large Angle and Spectrometric Coronagraph (LASCO; Brueckner et al. 1995) aboard the Solar and Heliospheric Observatory (SOHO; Domingo et al. 1995)). The observations at pre-eruptive phase are shown in Figure 1.

The magnetic field is observed by the Helioseismic and Magnetic Imager (HMI; Schou et al. 2012) and the product of Spaceweather HMI Active Region Patch (SHARP) series (Bobra et al. 2014; Hoeksema et al. 2014) is usually applied to magnetic field extrapolation. For data labeled with 'hmi.sharp_cea_720s' as displayed in panel (a), it performs the projection and remapping of the observed vector magnetic field onto the heliographic Cylindrical Equal-Area (CEA) coordinate system (Sun 2013), and an equal pixel size (0.36 Mm) is derived in both longitude (or X) and latitude (or Y) direction.

Images of seven EUV channels from Atmospheric Imaging Assembly (AIA; Lemen et al. 2012) are shown in panels (b)–(h). An overall bright sigmoid structure is clearly seen in AIA 94 Å even at the pre-eruptive phase, while double J-shaped feature is also identified in other EUV wavelengths. Specifically, the overall sigmoid in AIA 94 Å seems to consist of two separated parts, and filament fibrils are found in other wavelengths. The overall sigmoid structure has been reproduced with var-

ious extrapolations (Zhao et al. 2016; Kilpua et al. 2021) while the fine structures, e.g., the dark fibrils, have no apparent correspondences in the obtained 3D magnetic field.

2.2. MHS

The MHS model is developed by Zhu & Wiegelmann (2018) and optimized by Zhu et al. (2020a) and Zhu & Wiegelmann (2022). The latest version of the model (Zhu & Wiegelmann 2022), which considers MHS state in the lower atmosphere and force-free field in the upper atmosphere, is applied in the present work to obtain 3D magnetic field. The MHS model follows the MHS equilibrium equation:

$$\frac{1}{\mu_0}(\nabla \times \mathbf{B}) \times \mathbf{B} - \nabla p - \rho g \hat{z} = 0, \text{ satisfying } \nabla \cdot \mathbf{B} = 0. \quad (1)$$

where \mathbf{B} , p , ρ , are the vector magnetic field, plasma pressure and plasma density, while g and μ_0 denote the gravitational acceleration and vacuum permeability, respectively. More details can be found in Zhu & Wiegelmann (2022).

To reproduce the 3D magnetic field of AR 12158 with the MHS model, the vector magnetogram from SHARP CEA is adopted as the photospheric boundary as the MHS model is established in the Cartesian coordinate system. The radial component (B_r) of the photospheric magnetic field, which has original size of 532×564 pixel² with uniform pixel size of 0.36 Mm, is shown in Figure 1(a). A volume with size of $444 \times 312 \times 200$ pixel³ is extracted from extrapolation results, and the bottom boundary is shown by the dashed box in Figure 1(a).

2.3. CFITS

Under the assumption of force-free field, the forces from plasma gravity and pressure gradient are neglected in the solar atmosphere. Under such condition, the second and third terms in the MHS equation (Equation (1)) vanish and only the term of magnetic force remains, namely $\mathbf{J} \times \mathbf{B} = 0$. Various mathematical methods have been proposed to resolve the force-free equation, such as the optimization method (Wheatland et al. 2000; Wiegelmann 2004), the Grad–Rubin method (Grad & Rubin 1958) and others that have been mentioned in Section 1.

By adopting the Grad–Rubin method, Zhao et al. (2016) extrapolated the 3D magnetic field with the code of Current-Field Iteration in Spherical Coordinates (CFITS; Gilchrist & Wheatland 2014). The boundary condition is derived from the 720s SHARP series and is mapped from native helioprojective-Cartesian coordinates to heliographic coordinates at the photosphere.

¹ https://cdaw.gsfc.nasa.gov/CME_list/

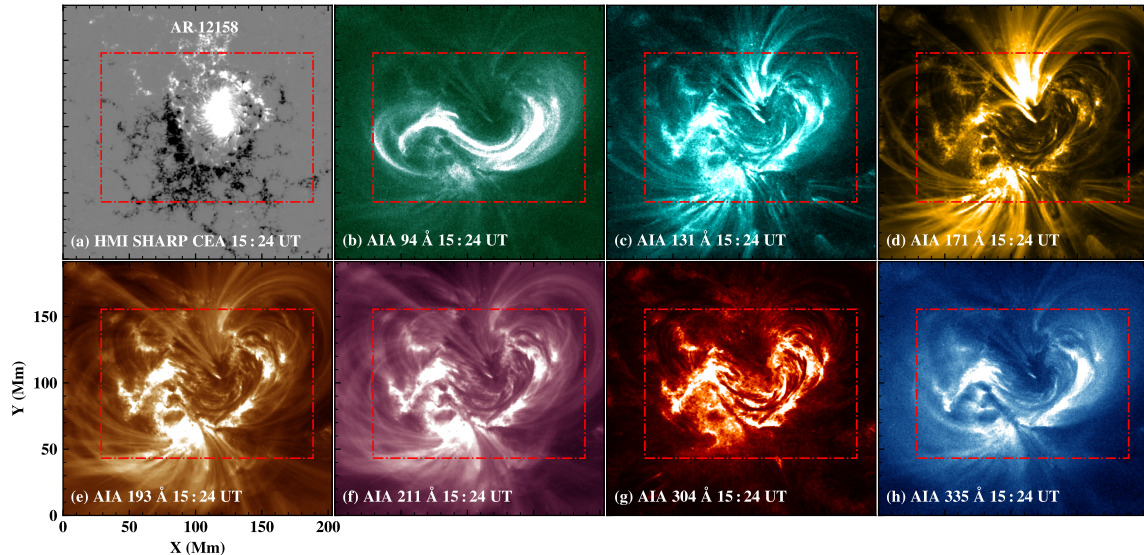


Figure 1. SDO observations of AR 12158 at 15:24 UT on 2014 September 10. Panel (a) shows the SHARP CEA remapped line-of-sight (LOS) magnetogram from SDO/HMI. Panels (b)–(h) show images of seven EUV channels from SDO/AIA. All the images are coaligned, and the red dashed boxes denote the major domain for the analyses in Section 3. An associated animation of panels (b)–(h) is available. The animation shows the evolution of various features such as sigmoid, hot channel, flare ribbon and the possible magnetic braiding during the period from 12:00 UT to 17:20 UT. The animation duration is about 64 s. (An animation related to this figure is available.)

After binning down and interpolation, the domain for extrapolation includes a spherical-polar coordinate mesh with $304 \times 273 \times 256$ points in the longitude, latitude and radial directions, which approximately has a uniform spacing of about 0.7 Mm, 0.7 Mm, 1.1 Mm, respectively.

Investigations (e.g., DeRosa et al. 2015; Thalmann et al. 2022) show that the extrapolation results might be affected by the spatial resolution, the geometry, the extrapolation method and other factors, and the most straight forward way to do the comparison is to use codes in the same geometry and exactly the same spatial resolution when it is possible. However, the MHS extrapolation method requires, in principle, a high spatial resolution boundary data which, in the present work, is not preprocessed, while the CFITS method is intrinsically developed based on spherical coordinate and uses a preprocessed boundary. Although the two extrapolations have different geometry, spatial resolution and bottom boundary, we think the comparison is still meaningful for the following reasons: 1) the active region that we investigated is located near the solar disk center which minimizes the geometry effect. In the following comparison, solutions based on different geometries are aligned with each other through coordinate transformation with the aid of the world coordinate system (WCS; Thompson 2006). 2) DeRosa et al. (2015) had a comprehensive discussion of the influence of spatial resolution on various NLFFF extrapolation. The Figure 6 of their

article shows that the calculated energies are mainly determined by the extrapolation method, and the effect of resolution is small. They also found that the field line trajectories calculated by the same extrapolation method appear quite similar for all resolutions. In addition, Thalmann et al. (2022) also analyzed the effect of spatial sampling on extrapolation results, and concluded that spatial sampling brings relatively small differences compared to factors such as applying different NLFFF methods.

3. RESULTS

3.1. Magnetic field and the pre-eruption brightenings

The brightenings of the sigmoid structure before eruption have been identified in various observations (McKenzie & Canfield 2008; Zhang et al. 2012; Vemareddy & Zhang 2014; Cheng et al. 2014; Cheng & Ding 2016) and also in the present work (see movie of Figure 1). They are suspected to be associated with magnetic reconnection, which is crucial for understanding the initiation and eruption of the flux rope system. The MHS model has an advantage in constructing the low-lying magnetic field lines, which enables a comparison between the pre-phase reconnection and the magnetic field in the low atmosphere. The reconstructed magnetic field from MHS model is analyzed in detail to show its correspondence with the brightenings in AIA observations.

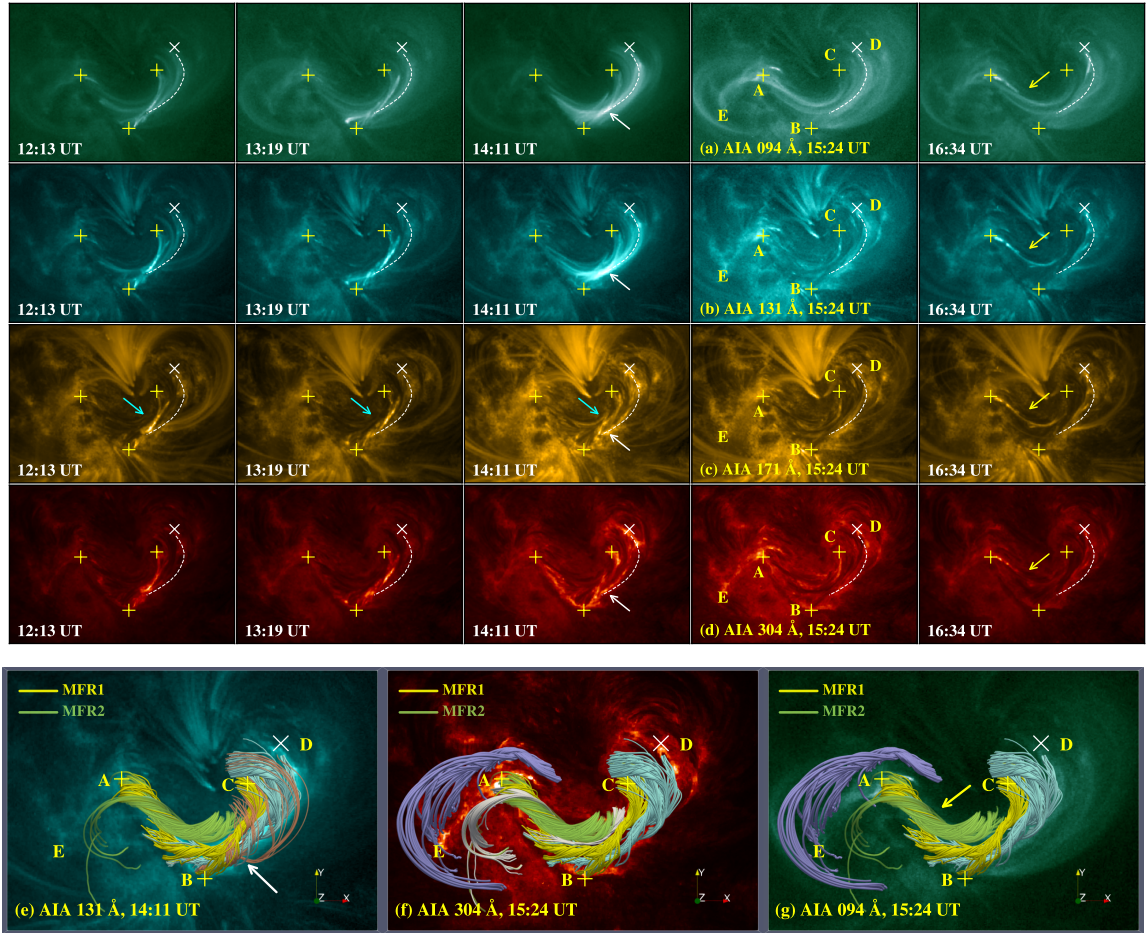


Figure 2. SDO observations at multiple time steps and the reconstructed magnetic field. Top panels: time evolution of the event in EUV images in 94, 131, 171, and 304 Å at five time steps (with 1 hour cadence) before the X-class flare. Bottom panels: the reconstructed magnetic field from MHS at 15:24 UT are overlaid on the AIA images at 14:11 UT for 131 Å, 15:24 UT for 304 Å and 94 Å for comparison. Different colors show the magnetic field lines with different connectivity. The plus signs and dash lines in the top and bottom parts are labeled for the reference of the locations for different connectivity.

In Figure 2, the EUV images at five selected time steps with a cadence of 1 hour are displayed in the top panels from left to right. The field lines from MHS model are shown in the bottom panels (e)–(g), with different field line systems overlaying on different features observed in AIA 131Å, 304Å, 94Å from left to right. The plus signs are added and annotated with ‘A’–‘E’ for identifying the locations of different features.

From 12:13 UT to 14:11 UT, the bright structure between B and C (pointed by the cyan arrows) evolves gradually. Enhanced emission (pointed by white arrows) is found in AIA 94 and 131 Å at 14:11 UT through a winding influence at 13:19 UT. The winding is also identified in AIA 171 and 304 Å while the induced emission enhancement is relatively weak. The sigmoid structure starts to brighten at 15:24 UT in AIA 94 Å, and a slender thread of brightening (pointed by yellow arrows) becomes visible in AIA 131, 171, 304 Å at 16:34

UT. The observed sophisticated evolution before the eruption may imply the existence of complex magnetic structure in the active region, such as the braiding magnetic field lines (Parker 1983; Berger & Asgari-Targhi 2009; Cirtain et al. 2013; Pontin et al. 2017) and the multi-flux-rope system (Awasthi et al. 2018). The relevant field lines are displayed in the bottom panels, with different connectivities shown with different colors for a better demonstration. In general, there are two main flux ropes represented by the field lines in yellow (MFR1) and green (MFR2) respectively. Ambient field lines that intimately coupled with the flux rope are displayed in purple, cyan and orange.

The field lines in cyan, which are beneath MFR1 for the left part and over-wrapping the latter at the right end, correspond to the dark region between C and D in AIA 304 Å (see panel (f)). The combination of MFR1 and field lines in cyan may represent the emission en-

hancement of AIA 94, 131Å at 14:11 UT. The region indicated by the white arrow in panel (e), which has over-wrapping field lines in orange on top of the MFR1 and field lines in cyan, may be responsible for the braiding features before 14:11 UT.

The primary part of MFR2 (field lines in green) is cospatial with the slender emission between A and B at 16:34 UT, and the left extension tends to outline the loop between A and E of AIA 94 Å. It implies the early stage of the hot channel suggested by Cheng et al. (2015) and the pre-existing MFR by Zhou et al. (2016).

In addition, the right branch of MFR1 between B and C seems to be consistent with the other dark stripe that is next to the aforementioned predominant one between C and D in AIA 304 Å. The field lines in purple have their feet anchored near the bright belt between A and E of AIA 304 Å, while the loops themselves tend to coincide with the outer loops of AIA 94 Å as shown in panel (g).

The comparison between magnetic field lines of MHS and observations of AIA images seems to reveal the good correspondence, suggesting the effectiveness of MHS assumption in recovering the fine structures of sigmoid system in observations.

3.2. EUV Eruptive Features and QSLs

As shown in Figure 2 and Figure 4, a two-flux-rope dominated system has been obtained by the MHS model while only one coherent flux rope is obtained in Zhao et al. (2016). The correspondence between the observations and the magnetic field of the MHS model in the aspect of pre-eruption brightening is already demonstrated in Section 3.1. To show its performance in inferring the eruptive features, such as flare ribbons and hot channels, the squashing factor Q are calculated for the MHS model and the results are shown in Figure 3.

The Q factor measures the gradients of magnetic connectivity in a volume, and the region with large Q value is defined as quasi-separatrix layer (QSL, Démoulin et al. 1996; Titov et al. 2002), which separates the region of distinct flux systems. Hence, Q map is a good indicator for ascertaining the characteristic structure of magnetic field. The method for calculating the Q factor can be found in Zhao et al. (2014) and can also refer to a FORTRAN parallel routine from Liu et al. (2016)².

The flare ribbons in AIA 304 Å are displayed in Figure 3(a) and the sigmoidal hot channels in AIA 94 Å are shown in Figure 3(b). The calculated Q maps at

the photosphere are displayed in Figures 3(c) and 3(d), while those along the vertical dot-dashed lines in Figures 3(c) and 3(d) are shown in Figures 3(e) and 3(f), with top panels for CFITS and bottom panels for MHS.

A detailed analysis of the 3D magnetic topology based on CFITS can be found in Zhao et al. (2016). Briefly, the footprints of QSLs at the photosphere (Figure 3(c)) are identified to match the position and shape of the double J-shaped flare ribbons at the beginning of the flare. There are several different magnetic connectivities viewed from the Q map in Figure 3(e). The inner centered small circle represents the core part of MFR0 with a larger twist, while its periphery is wrapped by a relatively weakly twisted magnetic structure. In addition, a hyperbolic flux tube (HFT) configuration appears at the intersection of QSLs with an altitude about 5 Mm, indicating the possible location of reconnection.

For the results obtained from the MHS extrapolation, S-shaped QSLs are generally identified in Figure 3(d). The contours of Q are overlaid on AIA 304 and 94 Å in Figures 3(a) and 3(b), respectively. The S-shaped QSLs generally coincide with the hot channel (L1) in AIA 94 Å and its hook parts roughly match the brightenings of the flare ribbons (R1 and R2) in AIA 304 Å.

In the vertical slice in Figure 3(f), an inner circle-shaped QSL, which indicates a strongly twisted MFR (MFR1), is wrapped by the outer QSLs. The height of MFR1 is about 8 Mm, which is lower than MFR0 that derived by CFITS. A second main flux rope (MFR2) is located adjacent to MFR1 and the main body is also outlined with a dashed line. The boundary of MFR2 is not as apparent as MFR1 in the Q map, which is due to the slice location. Moreover, there are high Q regions at the bottom below 5 Mm, yet the existence of HFT structure cannot be distinguished effectively, which may imply that the possible reconnection may distribute in a diffuse region, different from the results of CFITS.

3.3. Magnetic-field Configuration and QSLs

Correspondence between QSLs and magnetic configuration is explicitly revealed in the top three rows for both models in Figure 4 from 3D perspective. As the QSLs at the vertical slice have tremendous fine structures, we have used a vertical black-white sketch, as shown in the upper left and upper right corner of panels (a) and (e) respectively, as a proxy to better display the correspondence. The sketches are obtained by extracting the main structures associated with the magnetic flux ropes as we have found and annotated with dashed lines in Figures 3(e) and 3(f). The outer part of the flux rope (MFR0 and MFR1) is displayed with black while the inner part inside is shown with white. As no fine structures are

² <http://staff.ustc.edu.cn/~rliu/qfactor.html> or an updated site <https://github.com/el2718/FastQSL> according to Zhang et al. (2022)

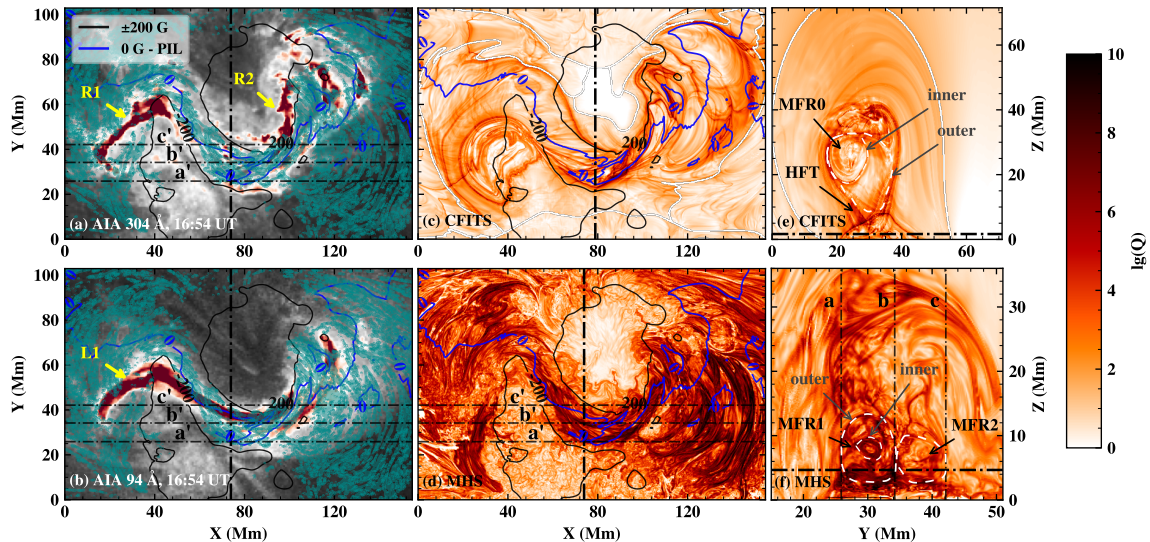


Figure 3. Comparison between the eruptive features and the calculated squashing factor of the magnetic field. AIA 304 and 94 Å images are shown in panels (a) and (b). The 2D distributions of QSLs from the MHS model are displayed in panels (d) and (f) while those from CFITS (more details see Zhao et al. 2016) are shown in panels (c) and (e) for comparison. The contours of QSLs in panel (d) are overlaid on panels (a) and (b) in green with $\lg(Q) = 5.5$. The blue and dark contours in panels (a) – (d) show the radial magnetic field from bottom boundary of CFITS, with levels of 0 and ± 200 G. The vertical dot-dashed lines in panels (a), (b) and (d) denote the slice position of panel (f) while the one in panel (c) denotes the slice position of panel (e). The horizontal dot-dashed lines in panels (e) and (f) show the height where the QSLs are sampled and displayed in panels (c) and (d), respectively. The dot-dashed lines annotated with a, b and c in panel (f) outline the region of MFR1 and MFR2 in the direction of Y-axis. Their photospheric correspondences are annotated with a', b', c' in panels (a), (b), (d), which outline the counterpart of the flux rope projection.

identified to be associated with MFR2, the whole flux rope region is shown with black. The annotations in the sketches are exactly the same as in Figures 3(e) and 3(f). The colors of the field lines in Figures 4(a)–(d) and 4(e)–(g) are coded with the twist number that is calculated through one common axis, i.e., MFR0 axis and MFR1 axis respectively. As we also calculate the twist numbers of MFR1 and MFR2 according to each axis respectively, the field lines in panel (h) are coded with two sets of twist number. More details of the twist number calculation is described in Section 3.4.

The magnetic field lines from CFITS are shown in the left column panels of Figure 4. The general distribution is shown in Figures 4(a) and 4(b) with different viewing angles. The selected low-lying field lines that beneath the HFT structure are displayed in Figure 4(c), where two sets of J-shaped field lines are clearly identified. The separated J-shaped structures are connected into one twisted S-shaped structure at higher height (see Figures 4(a) and 4(b)), which corresponds to the observed coronal sigmoid structure in SDO/AIA (Zhao et al. 2016). Such result conforms to the conventional magnetic scenario of pre-eruptive MFR (e.g., Jiang et al. 2021).

The field lines from the MHS model are shown in the right column panels of Figure 4. More complex connectivity is obtained due to the plasma forces from pres-

sure gradient and gravity. The magnetic field lines in the lower altitude (the aforementioned diffuse regions of possible reconnection from the distribution of QSLs) are roughly along the PIL. As shown in Figures 4(f) and 4(g), they also have the braiding characteristics and a coupling with the axis of MFR1 to a certain extent.

The core field lines of the flux rope MFR0 from CFITS are displayed in Figure 4(d), while those of flux ropes MFR1 and MFR2 from MHS are displayed in Figure 4(h). Around the regions of MFRs indicated by the QSLs as shown in the black-white sketch, a slightly smaller twist is confirmed for MFR2, which is located in the north of the highly twisted MFR1.

The above results explicitly show that, unlike the standard single-core MFR appearing in CFITS extrapolation, the sigmoidal configuration obtained in MHS primarily consists of two independent but slightly coupled twisted MFRs. The latter one, together with the ambient field lines, correspond well to the double J-shaped hot channels in AIA 94 Å as shown in Figure 2(g).

3.4. MHD instabilities

The helical kink instability (KI; Török et al. 2004) and torus instability (TI; Kliem & Török 2006), as two basic mechanisms of ideal MHD instability, are usually invoked to be responsible for triggering and driving the

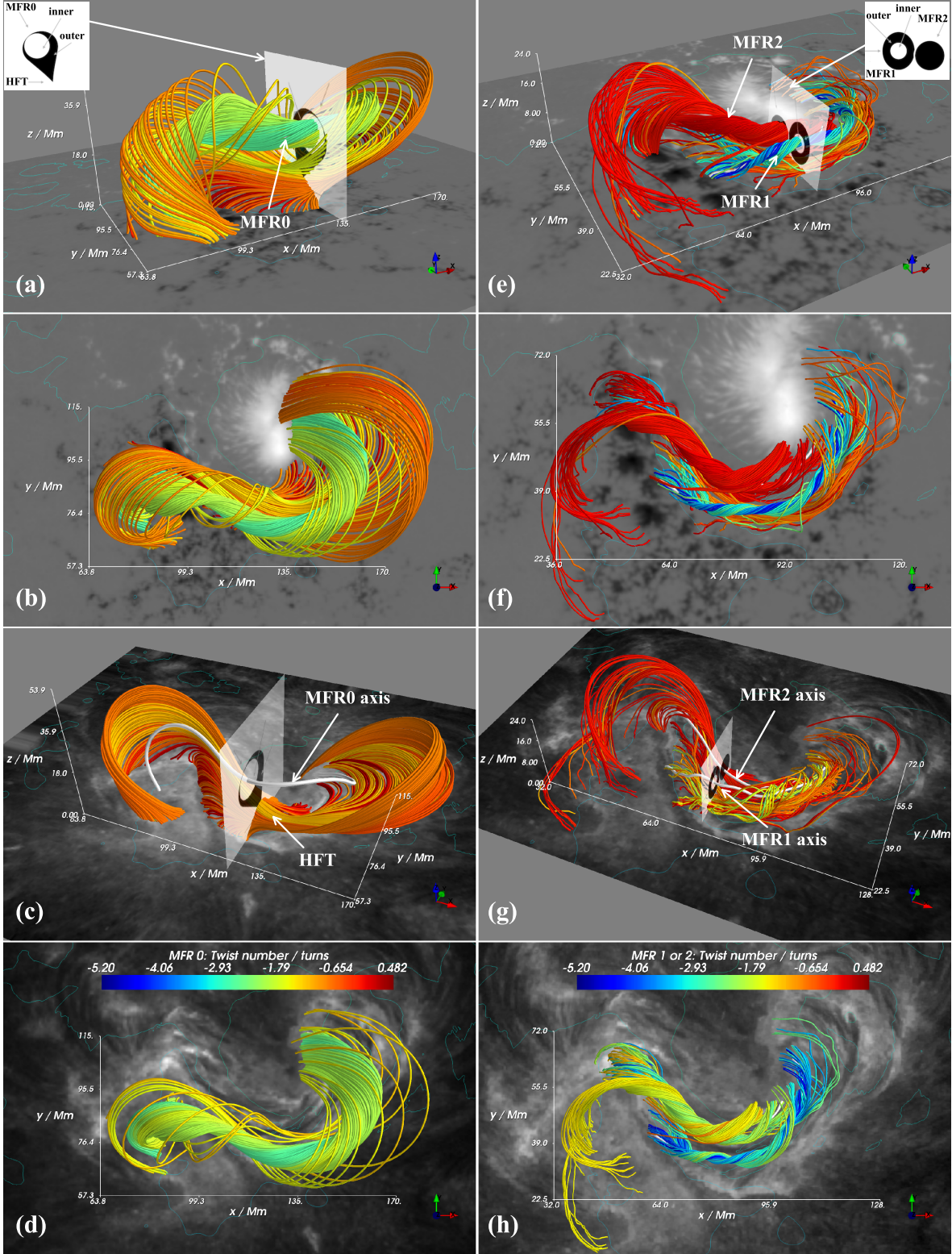


Figure 4. Magnetic connectivity and twist number of the flux rope system are displayed. CFITS result is shown in the left column panels and MHS on the right. All field lines are colored with the twist number. One common axis is selected for calculating the twist number in panels (a)–(g), while two separate axes, i.e., MFR1 axis and MFR2 axis, are adopted in panel (h) for calculating the twist number of MFR1 and MFR2, respectively. The 2D vertical slices with black-white sketch as shown in the corners of panels (a) and (e) are inserted in panels (a) and (c), (e) and (g) respectively with a view angle of 3D for emphasizing the connectivity.

MFR eruption, and are characterized by the parameters of twist number and decay index, respectively.

3.4.1. Twist Number

The KI suggests that the instability is triggered when the twist (Berger & Prior 2006) of the MFR exceeds a critical value T_c (well-known as ~ 1.25 turns in a force-free MFR suggested by Hood & Priest 1981). Based on Berger & Prior (2006), there are two typical definitions for the twist number. One measures the number of turns between two infinitesimally close magnetic field lines winding about each other and a fast code is developed by Liu et al. (2016) to calculate the twist in a volume. The other defines the twist number as the field lines wind about a common axis. The twist density of a curve $\mathbf{y}(s)$ around the smooth common axis curve $\mathbf{x}(s)$ is defined as

$$\frac{d\Phi}{ds} = \frac{1}{2\pi} \mathbf{T}(s) \cdot \mathbf{V}(s) \times \frac{d\mathbf{V}(s)}{ds}, \quad (2)$$

where s measures arc length from an arbitrary starting point on $\mathbf{x}(s)$, while $\mathbf{T}(s)$ is the unit tangent vector to $\mathbf{x}(s)$, and $\mathbf{V}(s)$ is the unit vector normal to $\mathbf{T}(s)$ pointing from $\mathbf{x}(s)$ to $\mathbf{y}(s)$. The final twist number T is obtained by integrating Equation (2) along the axis $\mathbf{x}(s)$.

The application of the latter method is to find a common axis among the magnetic field lines at the first step, and then to calculate the twist number of each curve around the axis. The axis and computational region are determined naturally by QSLs as they could depict the main body of an MFR (Guo et al. 2013, 2017b, 2021).

To better interpret the physical meaning, we adopt the latter definition to calculate the twist number with the code from Guo et al. (2010, 2013)³. As one coherent magnetic flux rope is reconstructed by CFITS, one common axis is inherently selected for calculating the distribution of the twist number. For the results from MHS, two individual magnetic flux ropes that are weakly coupled are obtained. One common axis, i.e., the axis of MFR1, has been tested for calculating the overall twist number and the results are shown in Figures 4(e)–4(g). As the main body of MFR2 departs from the axis of MFR1, a separate axis is therefore selected for MFR2 and the twist number is calculated separately for MFR1 and MFR2, as demonstrated in Figure 4(h).

For CFITS results, MFR0 has an average twist number of about $1.6 \sim 2$ turns, and a larger twist number up to about 2.6 turns in the core than the periphery. The highest twist number of MHS can reach 3 turns for

MFR2 and 5 turns for MFR1, with average values of about 1.6 and 3 turns, respectively. Both CFITS and MHS have larger twist numbers than T_c for triggering eruption. The quantitative results of twist number in the present work and other investigations are also listed in Table 1. Two cases are considered for both MFR0 and MFR1 in the present work, i.e., the internal core part and the one includes both the internal and external parts, due to the associated double-layer QSLs as shown in Figures 3(e) and 3(f).

3.4.2. Decay Index

The TI is suggested to have a significant effect on the eruption of an MFR due to the strapping force of the background field. Recently, a more relevant field ($B_{p,\text{ex}}$; Duan et al. 2019; Zhong et al. 2021), which is the component of the potential field that is perpendicular to both the axis and the erupting path of the MFR, is adopted for calculating the decay index. Like in other works (Bateman 1978; Jiang et al. 2014), the decay index of $B_{p,\text{ex}}$ is written as

$$n(r) = -\frac{d \log(B_{p,\text{ex}})}{d \log(r)}, \text{ or } n(r) = -\frac{r}{B_{p,\text{ex}}} \frac{dB_{p,\text{ex}}}{dr}. \quad (3)$$

The obtained decay indices of CFITS and MHS are shown in Figure 5. We find that CFITS and MHS have the decay index of about $1.3 \sim 1.7$ and $0.8 \sim 0.9$, respectively. Critical range of the decay index has been found within $0.8 \sim 1.5$ in Zhong et al. (2021) and within $0.5 \sim 2.0$ in Sun et al. (2022). According to such criteria, both models in the present work will be able to trigger torus instability. Nevertheless, comparing to the decay index from CFITS, the relative small index of MHS might be related with the low-lying flux rope, where the strapping field above could still be relatively strong.

3.5. Magnetic Energy and Helicity

Magnetic free energy and magnetic helicity, which are frequently investigated in previous studies, are also explored in the present work. Magnetic free energy is believed to be the upper limit of the energy release, while magnetic helicity essentially manifests the complexity of the magnetic field (Berger & Field 1984). As both calculations require the 3D potential field, the Laplace equation is numerically solved with Neumann boundary condition based on the Green's function method in cartesian geometry (Chiu & Hilton 1977; Wiegmann et al. 2005) and spherical geometry (see Appendix A). The details of the calculations are described as follows.

3.5.1. Magnetic Energy

³ https://github.com/njuguoyang/magnetic_modeling_codes

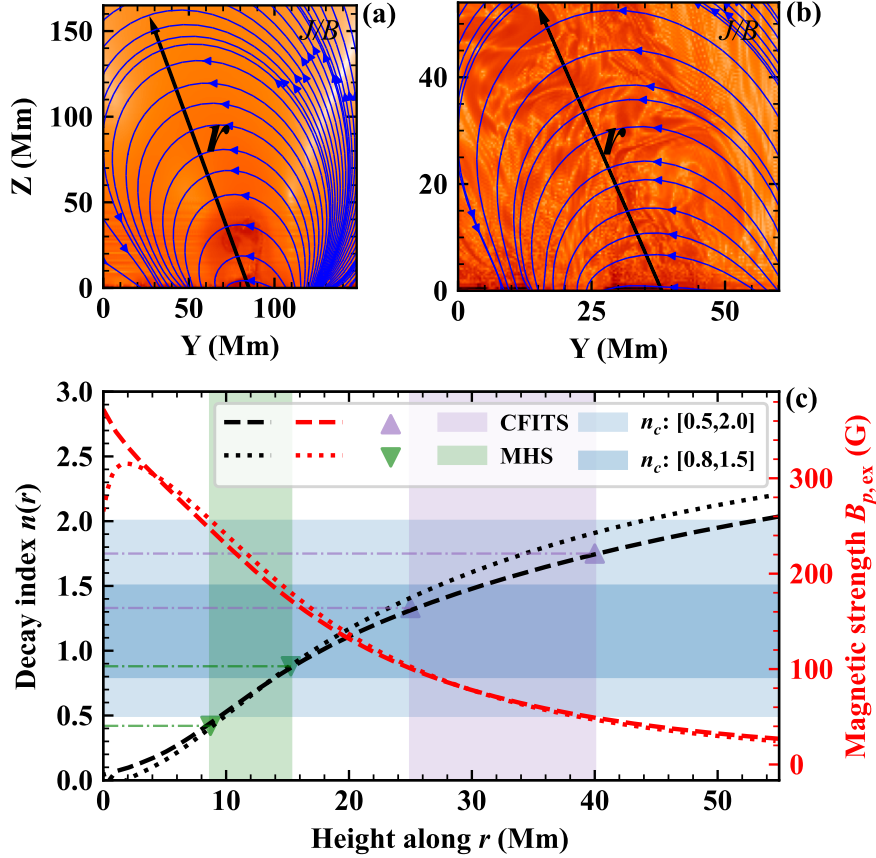


Figure 5. Comparison of decay indices. Panels (a) and (b) display the vertical slices of CFITS and MHS like those in Figures 3(e) and 3(f) but with J/B (current over field strength) as the background. The field lines in blue represent the projected component of the potential field on the vertical slice, and the oblique lines with arrows depict the directions r for calculating the decay index. Panel (c) shows the profiles of the decay index $n(r)$ (black lines) and of the strength of external poloidal magnetic field $B_{p,ex}$ (red lines), with dashed lines represent the CFITS model and dotted lines for the MHS model. The blue and light blue shaded areas denote the reference range of critical decay index n_c from Zhong et al. (2021) and Sun et al. (2022), respectively. The purple and green shaded areas show the rough height ranges of CFITS and MHS, from the MFR core to the apex along the direction of r . The lower and upper limits of decay index are marked by ∇ and \triangle for CFITS and MHS, respectively.

The energy stored in magnetic field that can power eruptions is the free energy, which is estimated as:

$$E_{\text{free}} = \int_V \frac{B^2}{8\pi} dV - \int_V \frac{P^2}{8\pi} dV = \int_V \frac{B^2 - P^2}{8\pi} dV, \quad (4)$$

where B and P are the strength of non-potential field and reference potential field respectively. The integrand denotes the energy density distributed over the computational domain V . By integrating energy density along LOS, a 2D distribution of free energy $E_{\text{free}}(x, y)$ is obtained as shown in Figures 6(a) and 6(d), and a similar demonstration was adopted by Mackay et al. (2011) and Jiang & Feng (2012). The results indicate that the free energy of CFITS is concentrated in the region where MFR0 is located, while MHS has high free energy distributed along MFR1 and MFR2, in addition to the sunspot region (also see Figure 6 for 3D renderings).

As discussed by Borrero & Ichimoto (2011) and Tiwari (2012), sunspots tend to be non-potential which implies that the existence of free energy, and the consideration of plasma effect in MHS model may also lead to free energy. Some negative values of free energy density exist for both methods, which might be due to the accuracy of the numerical methods to some extent, and other works (e.g., Mackay et al. 2011; Jiang et al. 2014) also discussed the possible physical sources.

3.5.2. Magnetic Helicity

Magnetic helicity, in its original definition, is the volume integral of the scalar product between vector potential and vector magnetic field. It measures the linkage of a bundle of magnetic field lines, and is related to the topological concepts such as Gauss linking number, and the usually used twist number and writhe number

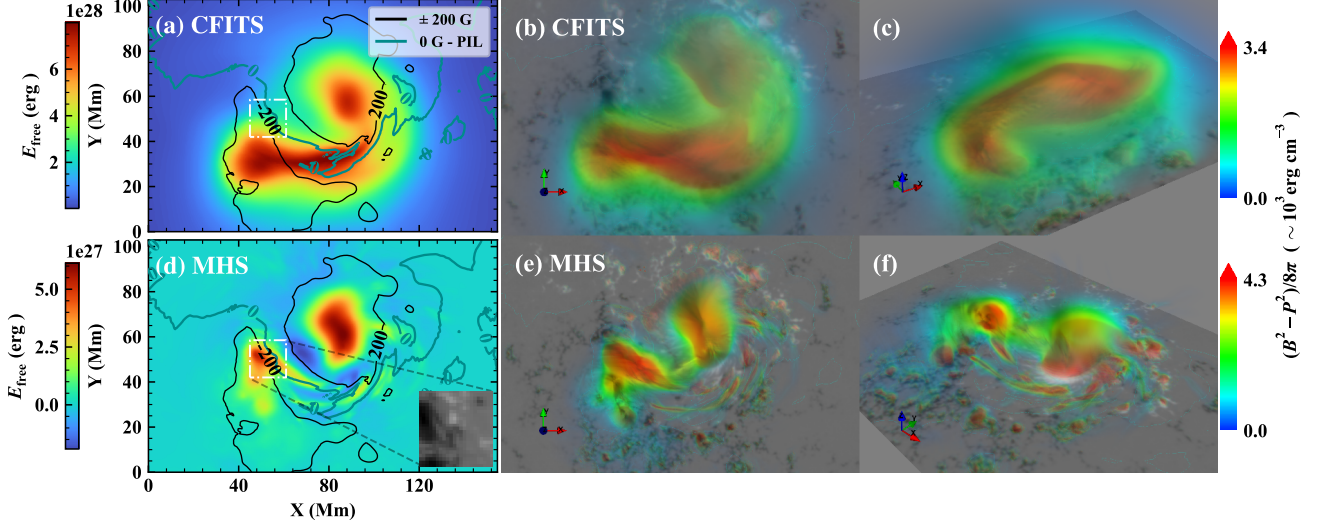


Figure 6. Distributions of free energy in 2D and 3D for CFITS (panels (a)–(c)) and MHS (panels (d)–(f)). The 2D maps in panels (a) and (d) display the integrals along Z direction with several layers covering the primary structure. The contours in cyan and dark show the LOS magnetic field from CFITS with levels of 0 and ± 200 G. The white dot-dashed boxes denote the site of shearing flow and cancellation suggested by Cheng et al. (2015). The 3D maps in the right four panels show the volume rendering of $(B^2 - P^2)/8\pi$.

(Berger & Field 1984; Moffatt & Ricca 1992; Berger & Prior 2006). For solar active region, relative magnetic helicity is given by Berger & Field (1984) and Finn & Antonsen (1985) for the domain above photosphere ($z > 0$):

$$H_m = \int_{z>0} (\mathbf{A} + \mathbf{A}_p) \cdot (\mathbf{B} - \mathbf{P}) dV, \quad (5)$$

where \mathbf{A} and \mathbf{A}_p are the vector potentials of \mathbf{B} and \mathbf{P} satisfying $\hat{\mathbf{n}} \cdot \mathbf{B}|_{z=0} = \hat{\mathbf{n}} \cdot \mathbf{P}|_{z=0}$ to keep H_m gauge invariant. This form of helicity calculation is also known as the finite volume method (Valori et al. 2012). More methods of helicity estimation are proposed, such as twist-number (TN), helicity-flux integration (FI), connectivity-based (CB), see Valori et al. (2016), Guo et al. (2017a) and Thalmann et al. (2021) for an overview. Like in previous works (DeVore 2000; DeVore & Antiochos 2000; Fan 2009), the expressions of \mathbf{A} and \mathbf{A}_p are written as under the DeVore gauge:

$$\mathbf{A}(x, y, z) = \mathbf{A}_p(x, y, 0) - \hat{\mathbf{z}} \times \int_0^z \mathbf{B}(x, y, z') dz', \quad (6)$$

$$\mathbf{A}_p(x, y, z) = \nabla \times \hat{\mathbf{z}} \int_z^\infty \varphi(x, y, z') dz', \quad (7)$$

where φ , as the Green's function solution for the Laplace's equation, is :

$$\varphi(x, y, z) = \frac{1}{2\pi} \iint \frac{B_z(x', y', 0)}{[(x-x')^2 + (y-y')^2 + z^2]^{1/2}} dx' dy'. \quad (8)$$

In practice, we further adopt a more performable form below with the aid of $\mathbf{P}(x, y, z) = -\nabla\varphi(x, y, z)$:

$$\mathbf{A}(x, y, z) = \mathbf{A}_p(x, y, 0) - \left(-\int_0^z B_y dz', \int_0^z B_x dz', 0 \right) \quad (9)$$

$$\mathbf{A}_p(x, y, z) = \left(\int_z^\infty -P_y dz', \int_z^\infty P_x dz', 0 \right). \quad (10)$$

Equations (6) to (10) are performed in Cartesian coordinates for MHS, while the spherical scheme for CFITS is available from Fan & Gibson (2007). The finite volume method as carried out above estimates a global quantity of magnetic helicity. One could refer to the relative field line helicity (e.g., Yeates & Page 2018; Moraitis et al. 2019a, 2021), which is developing vigorously in recent years, for a distribution investigation. To further obtain more physical meaningful results, two other methods are considered in the following.

3.5.3. Current-carrying Helicity and Twist Helicity

As shown in previous works (Berger 1999, 2003; Guo et al. 2017b), the helicity in a finite volume can be decomposed into two components, with one component representing the contribution from the magnetic field that carries local currents and the other component standing for the contribution from the potential field and magnetic field generated by local currents. The former component is called current-carrying helicity as H_J in the present work and is calculated as follows:

$$H_J = \int_V (\mathbf{A} - \mathbf{A}_p) \cdot (\mathbf{B} - \mathbf{P}) dV. \quad (11)$$

Solar eruptions often show highly twisted magnetic flux rope, which initiated a twist number method for the helicity calculation (Guo et al. 2010, 2013, 2017b). By neglecting the contribution from writhe, and also the one from the mutual helicity between magnetic flux rope and ambient field, the twist helicity is calculated as follows:

$$H_{\text{twist}} \approx T\Phi^2, \quad (12)$$

where $\Phi = \iint B_x dydz$ is the axial magnetic flux.

The current-carrying helicity and twist helicity are then obtained for both models and the values are shown in Table 1. It is found that $|H_{\text{twist}}|$ of CFITS and MHS is smaller than $|H_J|$, which probably due to the fact that the local current is not completely limited to the volume occupied by the MFR. However, $|H_{\text{twist}}|$ of MHS is much smaller than $|H_J|$ because MHS has two coupled MFRs and braiding with the surrounding magnetic field, thus the mutual helicity is underestimated in the computation. Meanwhile, H_{twist} is also affected by Φ^2 because of the smaller magnetic flux.

The role of magnetic helicity for indicating the solar eruptions has been extensively discussed (Toriumi & Park 2022). MHD simulations (e.g., Pariat et al. 2017; Zuccarello et al. 2018; Linan et al. 2018) suggest that helicity ratio, i.e., $|H_J|/|H_m|$ is a promising proxy of solar eruptivity. In observations, statistics (Gupta et al. 2021) and case studies (James et al. 2018; Moraitis et al. 2019b; Thalmann et al. 2019) using force-free modeling also show that $|H_J|/|H_m|$ has advantages in predicting the eruptive potential of a flaring AR. It is mainly characterized by the higher $|H_J|/|H_m|$ values (e.g., >0.1 in Gupta et al. 2021) for CME-productive active regions, and the reduction of $|H_J|/|H_m|$ during eruptions. In the present work, the helicity ratios given by CFITS and MHS are about 0.25 and 0.05, respectively. By inspecting the MHS result, we find that there are some positive values in the volume of integrand from equation (11), although the integral helicity of the entire computational volume is negative. The absolute ratio of the positive integral to the negative one of H_J is about 0.62, which naturally leads to a small value of current-carrying helicity integration as the two components are not treated separately. Such difference is inherently dependent on the two methods which reconstructing different magnetic configurations. Nevertheless, there are exceptions of the statistical threshold (Thalmann et al. 2021; Gupta et al. 2021) and whether there is a universal criterion for extrapolations with different assumptions, i.e., the force-free and non-force-free ones, requires further examinations with more samples (Moraitis et al. 2019b; Toriumi & Park 2022).

3.5.4. Comparison with previous results

As AR 12158 has been extensively studied in various aspects and with various extrapolation methods, we show the results present here and their associations with previous results. Cheng et al. (2015) investigated the shearing flow and magnetic cancellation in the region that is outlined with a white box in Figure 6(d). At the same region, we find that MHS covers conspicuous free energy, which can not be identified in the relevant distributions from CFITS. Half eruption that discussed in Shen et al. (2022) also supports the extrapolation result of MHS, which reconstructs two distinct flux rope systems with only MFR2 erupting.

Considering different extrapolation methods, a quantitative comparison is listed in Table 1 in the aspect of magnetic energy and magnetic helicity. Solution obtained with the CFITS has higher energies and helicities than that calculated using the MHS method, even in terms of the potential energy. Such result seems unusual since a rebinned magnetogram with a lower resolution usually leads to a lower potential energy due to missing of magnetic fluxes. However, this is not always true as revealed by DeRosa et al. (2015) who found, in their Figure 6, that the potential energy basically shows an oscillation pattern as the rebin factor changes. Although it is difficult to use exactly the same bottom boundary since different methods usually have different requirements on geometry and pre-processing, magnetic configurations and the relative values of magnetic energy and helicity are still informative for comparison. As shown in Figure 6, the free energy around the flux rope is dominated in the active region, therefore larger values of E_{free} would be expected for a more extended flux rope. This is precisely the case here that the integrals are large for CFITS which derives an extended flux rope while a more contracted flux rope is acquired by MHS who obtains small values of the integral. Table 1 also shows results from Duan et al. (2017) who compared different extrapolations with NLFFF code (CESE-MHD-NLFFF, by Jiang & Feng 2013) and non-force-free field code (NFFF, by Hu & Dasgupta 2008; Hu et al. 2010). Excluding NLFFF1, CFITS obtains larger free energy and relative helicity, comparing to the other methods. The obtained $E_{\text{free}}/E_{\text{pot}}$ is also large for CFITS, and such large value has been obtained in other works (e.g., Metcalf et al. 2008; Schrijver et al. 2008; Vemareddy 2019; Rudenko & Dmitrienko 2020; Zou et al. 2020). Overall, although the plasma forces bend the magnetic field lines to form a non-force-free configuration in MHS method, the above results demonstrate that the non-force-freeness does not necessarily bring in more energy or helicity, and the occupation of the obtained flux rope

might be important for the integral results of the free energy and relative helicity.

4. SUMMARY AND DISCUSSION

4.1. Summary

Magnetic field in the solar atmosphere, which is responsible for solar eruptions, interacts with plasma in nature, especially at the lower atmosphere such as the photosphere and lower chromosphere where plasma β is larger than 1. To construct a 3D magnetic field above the photosphere, which could imitate the observations in more details, it is necessary to consider the contribution of plasma, and the gravity and pressure gradient forces should be taken into account in the first step. In this paper, we reconstruct the magnetic field of AR 12158 by using the MHS extrapolation method and compare it mainly with the force-free field (CFITS method) from [Zhao et al. \(2016\)](#), in the aspects of magnetic topology and connectivity, MHD instabilities, magnetic energy and relative helicity. Additionally, the performance of MHS model for reproducing the observations in AIA EUV passbands are evaluated.

The EUV observations before eruption imply that AR 12158 contains abundant atmospheric structures, such as the S-shaped structure composed of two separated J-shaped segments in AIA 94 Å, the dark stripes in AIA 304 Å, and the twisted brightening structure in multi-wavelengths.

In terms of magnetic field, a single flux rope (MFR0) is reconstructed by CFITS, while MHS distinguishes two separate but weakly coupled flux rope systems (MFR1 and MFR2). MFR2 of MHS and MFR0 of CFITS have the similar twist number of $1 \sim 2$ turns, while MFR1 of MHS has an average twist of about 3 turns and a maximum one of about 5 turns for the core part. Sheared arcades have also been obtained for this active region by some other extrapolation methods (such as [Vemareddy et al. 2016](#); [Duan et al. 2017](#); [He et al. 2022](#)). For most extrapolation results, the sigmoid structure from the observation has a rough counterpart in the magnetic field. Among these extrapolations, the magnetic flux rope MFR2 of MHS is more likely in consistent with the hot channel suggested by [Cheng et al. \(2015\)](#). The mentioned site of shearing flow and cancellation corresponds to the location where the free energy from MHS are most concentrated, while no explicit correspondence can be found from other methods.

In terms of the overall asset, such as the total amount of free energy and relative helicity, MHS and CFITS, as well as other NLFFF and NFFF methods, derive values

on the same order of magnitude, i.e., $\sim 10^{32}$ erg and $\sim 10^{43}$ Mx² respectively.

The above results show that although the estimated total amount of energy and helicity are on the same order for different extrapolation methods, there are differences in the specific magnetic configuration, thus leading to different understanding of the eruption. It suggests that the force-free field models prevalently used nowadays enable a rough description of the active region magnetic field. Detailed magnetic structures, which are crucial for understanding the evolution of flux rope as well as the trigger of eruption at the initial phase, can be acquired from the MHS model with consideration of the plasma.

4.2. Further Discussion

High twist number is obtained from the MHS method while only sheared arcades or weakly twisted flux rope have been reproduced from other NLFFF methods. The validation of such high twist and the associated MHD instability are further discussed in this subsection.

4.2.1. High Twist Number

Based on the methodological tests, [Low \(1985, 1992\)](#) proposed an analytical MHS equation for solar active region. They found that the magnetic field lines become more complex with elongated and multi-helical features, when considering both field-aligned and cross-field electric currents in their model. It in principle demonstrates the effect of considering plasma when inferring the 3D magnetic field from photospheric magnetic field. [Zhu & Wiegmann \(2019\)](#) tested the MHS approach with radiative MHD simulation. They found that the twisted magnetic structure is well reconstructed by the MHS model, while the NLFFF ([Wiegmann 2004](#); [Wiegmann et al. 2006](#)) only show sheared lines.

In the aspect of observations, the rotation of sunspot may contribute to the high twist of magnetic field lines. Such contributions have been identified in [Vemareddy et al. \(2016\)](#) and [Brown & Walker \(2021\)](#) for AR 12158, and in AR 11943/11944 ([Duan et al. 2021](#)) for the flux rope structure. Twist number as high as 6 turns has been obtained in the latter case. Interplanetary magnetic cloud with high twist number (more than 10 turns per astronomical unit) is frequently observed at L1 point ([Wang et al. 2016](#)), indicating the eruptive counterpart near the sun may be highly twisted originally. In addition, the time-dependent data-driven simulation and in-situ measurements also show high twist number of the MFR structure from AR 12158 ([Kilpua et al. 2021](#)).

4.2.2. MHD instability

Table 1. Magnetic quantities derived from different methods

Model	E_{tot} (10^{32} erg)	E_{pot} (10^{32} erg)	E_{free} (10^{32} erg)	$E_{\text{free}}/E_{\text{pot}}$	H_{m} (10^{43}Mx^2)	H_{J} (10^{43}Mx^2)	H_{twist} (10^{43}Mx^2)	$\overline{ T_{\text{w}} }$ (outer/inner) (Turn)
CFITS	16.35	10.74	5.62	52.3%	-3.87	-0.96	-0.20 ± 0.05	MFR0, 1.62 ± 0.40 , 1.97 ± 0.29
MHS	11.15	9.90	1.25	12.7%	-1.57	-0.082	-0.007 ± 0.004	MFR1, 1.39 ± 0.92 , 3.06 ± 0.82 MFR2, 1.59 ± 0.40 ,
NLFFF1	11.5	11.7	-0.18	-1.5%	-1.60	-	-	≤ 1.0
NLFFF2	11.1	10.0	1.10	10.9%	-2.03	-	-	≤ 1.0
NFFF	14.8	11.8	3.02	25.6%	-2.36	-	-	≤ 1.0

NOTE—NLFFF1, NLFFF2, and NFFF are results from [Duan et al. \(2017\)](#), and their twist number are computed by the first definition. The NLFFF1 and NLFFF2 use unpreprocessed and preprocessed vector magnetograms as boundaries, respectively. The negative free energy in NLFFF1 arises probably due to inconsistency between the unpreprocessed magneogram and the force-free approximation.

MFR with large twist number is considered to be explosive due to kink instability. Both the theories and observations demonstrate that the critical twist number has a large range and is influenced by such as the external magnetic field, the plasma flow and plasma β (see discussion in [Guo et al. 2021](#)).

The maximum twist number ($|T|_{\text{max}}$) was found to vary across different flares events ([Liu et al. 2016](#)). Such parameter was employed by [Duan et al. \(2019\)](#) as the kink instability controlling parameter of the pre-flare MFRs in a statistical study. Their results demonstrate that flare events with $|T|_{\text{max}}$ exceeding its critical value ($|T|_{\text{c}}$) have a high possibility to erupt successfully. Lower limit and average values of $|T|_{\text{c}}$ from statistics are suggested to be 2 and 2.83 ± 1.31 turns respectively.

Meanwhile, previous works ([Dungey & Loughhead 1954](#); [Hood & Priest 1979](#); [Bennett et al. 1999](#); [Baty 2001](#)) estimated the critical value of a uniform twisted MFR with axial length L and minor radius a is $T_{\text{c}} = \frac{\omega_{\text{c}}L}{2\pi a}$, suggesting a higher value for thinner MFR. Considering the non-force-free state in the present work, the parameter ω_{c} , which depends on detailed configuration of an MFR, is selected to be around 2 ([Dungey & Loughhead 1954](#); [Bennett et al. 1999](#); [Wang et al. 2016](#)). With the aspect ratio L/a being estimated as 18 for MFR1, we derive a critical twist of about 5.7 turns which is greater than the $|T|_{\text{max}} \approx 5$ turns of MFR1.

Nevertheless, there might be uncertainty in estimating T_{c} with the above formula. First, the reconstructed MFRs do not perfectly satisfy the original definition of T_{c} in geometry, thus bring in an estimation error of L/a . Second, the force-free and non-force-free state are not two opposite conditions so that each corresponds to a fixed ω_{c} . Furthermore, from the investigation of 115 MCs, [Wang et al. \(2016\)](#) suggested $w_{\text{c}} = 2$ is probably a reasonable criteria or upper limit for the unstableness of

MFRs, while the lower limit and the general value could be 0.2 and 0.6, respectively. According to [Wang et al. \(2016\)](#), we reconsider the relevant threshold of MFR1 and get 0.6, 1.7, 2.9 turns of T_{c} for ω_{c} of 0.2, 0.6, 1.0, respectively.

4.2.3. Possible Braiding

The braiding mechanism of magnetic field lines provides a scheme for energy dissipation and coronal heating in the parker-type nanoflaring scenarios ([Parker 1988](#); [Berger & Asgari-Targhi 2009](#); [Aschwanden 2019](#); [Pontin & Hornig 2020](#)). [Cirtain et al. \(2013\)](#) reported the braided fine structure from Hi-C high-resolution observations. [Awasthi et al. \(2018\)](#) also revealed the pre-eruptive reconnection in a braided multi-flux-rope system. In addition, [Aschwanden \(2019\)](#) suggested that the braiding required by parker-type scenarios prefers a non-force-free environments, such as in the chromosphere and transition region. In the present work, the MHS technique reproduces magnetic correspondence of the distinct braiding features, which is not produced by the force-free field method. Therefore, the comparison between MHS and CFITS indicates that the MHS method might be more conducive to reproduce fine structures such as the braided characteristics.

Acknowledgements. We thank the anonymous referee and scientific editor Dr. Manolis K. Georgoulis for their valuable suggestions. We thank Dr. Yingna Su for an internal review of this paper. Data from observations are provided by NASA/SDO and the HMI and AIA science teams. We also thank the open-source tools ([Mayavi](#) and [ParaView](#)) for 3D scientific data visualization. This work is supported by Open Research Program No. KLSA202112 of CAS Key Laboratory of Solar Activity. J.Z. acknowledges the sup-

ports by National Natural Science Foundation of China, Grant No. 12233012, 11503089, U1731241 and Chinese Academy of Science Strategic Pioneer Program on Space Science, Grant No. XDA15052200, XDA15320103, XDA15320301. F.Y., J.Z., and Y.S. also acknowledge the National Natural Science Foundation of China (grant Nos. 11820101002). X.S. acknowledges finan-

cial support by National Key R&D Program of China (2021YFA1600503), NSFC grant 11790301, and mobility program (M-0068) of the Sino-German Science Center. Y.G. was supported by NSFC (11773016, 11961131002, and 11533005) and 2020YFC2201201.

APPENDIX

A. GREEN'S FUNCTION FOR POTENTIAL FIELD IN SPHERICAL COORDINATES

Generally, current-free or potential magnetic field, which has a scalar potential $\phi(\mathbf{r})$ satisfying the Laplace equation $\Delta\phi = 0$, can be expressed as $\mathbf{P}(\mathbf{r}) = -\nabla\phi(\mathbf{r})$ (Sakurai 1982; Wiegelmann & Sakurai 2021). Therefore, to obtain potential field, the fundamental step is solving the Laplace equation with appropriate boundary conditions. We consider the line-of-sight (LOS) photospheric magnetic field $B_l(\mathbf{r}')$ as the Neumann boundary, then the solution of the Laplace equation can be written as the integral below:

$$\phi(\mathbf{r}) = \int_{S'} B_l(\mathbf{r}') G_N(\mathbf{r}, \mathbf{r}') dS', \quad (\text{A1})$$

where, G_N is the Green's function for Neumann boundary condition. In spherical geometry, G_N is written as (Sakurai 1982; Nemenman & Silbergleit 1999; Maclean et al. 2006):

$$G_N = \frac{1}{4\pi} \left[\frac{2}{|\mathbf{r} - \mathbf{r}'|} + \frac{1}{R} \ln \left(\frac{rR - \mathbf{r} \cdot \mathbf{r}'}{R^2 + R|\mathbf{r} - \mathbf{r}'| - \mathbf{r} \cdot \mathbf{r}'} \right) \right] \quad (\text{A2})$$

$$= \frac{1}{4\pi} \left[\frac{2}{\sqrt{r^2 - 2rR\cos\omega + R^2}} + \frac{1}{R} \ln \left(\frac{r(1 - \cos\omega)}{R + \sqrt{r^2 - 2rR\cos\omega + R^2} - r\cos\omega} \right) \right], \quad (\text{A3})$$

where, $\mathbf{r} = (r, \theta, \varphi)$ and $\mathbf{r}' = (R, \theta', \varphi')$ are the position vectors of the field point and the source, respectively, and ω is the angle between \mathbf{r} and \mathbf{r}' .

We know that $\mathbf{P}(r, \theta, \varphi) = -\nabla\phi(r, \theta, \varphi)$, and the coordinate parameters (r, θ, φ) are independent variables for the integral Equation (A1). Therefore, the solution of potential field is rewritten as:

$$\mathbf{P}(r, \theta, \varphi) = - \int_{S'} B_l(\mathbf{r}') \nabla G_N(\mathbf{r}, \mathbf{r}') dS', \quad (\text{A4})$$

where the elementary surface area $dS' = R^2 \sin\theta' d\theta' d\varphi'$, and three components of $\nabla G_N(\mathbf{r}, \mathbf{r}')$ in r , θ and φ directions are derived as follows:

$$G_r = -\frac{1}{4\pi} \frac{r^2 - R^2}{r|\mathbf{r} - \mathbf{r}'|^3}, \quad (\text{A5})$$

$$G_t = -\frac{1}{4\pi} \left[\frac{2rRC_1}{|\mathbf{r} - \mathbf{r}'|^3} + \frac{1}{R} \left(\frac{rC_1 + \frac{rRC_1}{|\mathbf{r} - \mathbf{r}'|}}{|\mathbf{r} - \mathbf{r}'| + R - r\cos\omega} - \frac{C_1}{1 - \cos\omega} \right) \right] \frac{1}{r}, \quad (\text{A6})$$

$$G_p = -\frac{1}{4\pi} \left[\frac{2rRC_2}{|\mathbf{r} - \mathbf{r}'|^3} + \frac{1}{R} \left(\frac{rC_2 + \frac{rRC_2}{|\mathbf{r} - \mathbf{r}'|}}{|\mathbf{r} - \mathbf{r}'| + R - r\cos\omega} - \frac{C_2}{1 - \cos\omega} \right) \right] \frac{1}{r \sin\theta}, \quad (\text{A7})$$

where, $|\mathbf{r} - \mathbf{r}'| = \sqrt{r^2 - 2rR\cos\omega + R^2}$, and

$$\cos\omega = \cos\theta\cos\theta' + \sin\theta\sin\theta'\cos(\varphi - \varphi'), \quad (\text{A8})$$

$$C_1 = \sin\theta\cos\theta' - \cos\theta\sin\theta'\cos(\varphi - \varphi'), \quad (\text{A9})$$

$$C_2 = \sin\theta\sin\theta'\sin(\varphi - \varphi'). \quad (\text{A10})$$

In fact, Sadykov & Zimovets (2014) also provided another expression of numerical solution for calculating the potential magnetic field in solar active regions in a spherical geometry.

REFERENCES

- Amari, T., Boulmezaoud, T. Z., & Aly, J. J. 2006, *A&A*, 446, 691, doi: [10.1051/0004-6361:20054076](https://doi.org/10.1051/0004-6361:20054076)
- Antiochos, S. K. 1987, *ApJ*, 312, 886, doi: [10.1086/164935](https://doi.org/10.1086/164935)
- Aschwanden, M. J. 2019, *ApJ*, 874, 131, doi: [10.3847/1538-4357/ab0b42](https://doi.org/10.3847/1538-4357/ab0b42)
- Awasthi, A. K., Liu, R., Wang, H., Wang, Y., & Shen, C. 2018, *ApJ*, 857, 124, doi: [10.3847/1538-4357/aab7fb](https://doi.org/10.3847/1538-4357/aab7fb)
- Barthol, P., Gandorfer, A., Solanki, S. K., et al. 2011, *SoPh*, 268, 1, doi: [10.1007/s11207-010-9662-9](https://doi.org/10.1007/s11207-010-9662-9)
- Bateman, G. 1978, *MHD instabilities*
- Baty, H. 2001, *A&A*, 367, 321, doi: [10.1051/0004-6361:20000412](https://doi.org/10.1051/0004-6361:20000412)
- Bennett, K., Roberts, B., & Narain, U. 1999, *SoPh*, 185, 41, doi: [10.1023/A:1005141432432](https://doi.org/10.1023/A:1005141432432)
- Berger, M. A. 1988, *A&A*, 201, 355
- . 1999, *Plasma Physics and Controlled Fusion*, 41, B167, doi: [10.1088/0741-3335/41/12B/312](https://doi.org/10.1088/0741-3335/41/12B/312)
- . 2003, in *Advances in Nonlinear Dynamics*, ed. A. Ferriz-Mas & M. Núñez, 345–374, doi: [10.1201/9780203493137.ch10](https://doi.org/10.1201/9780203493137.ch10)
- Berger, M. A., & Asgari-Targhi, M. 2009, *ApJ*, 705, 347, doi: [10.1088/0004-637X/705/1/347](https://doi.org/10.1088/0004-637X/705/1/347)
- Berger, M. A., & Field, G. B. 1984, *Journal of Fluid Mechanics*, 147, 133, doi: [10.1017/S0022112084002019](https://doi.org/10.1017/S0022112084002019)
- Berger, M. A., & Prior, C. 2006, *Journal of Physics A Mathematical General*, 39, 8321, doi: [10.1088/0305-4470/39/26/005](https://doi.org/10.1088/0305-4470/39/26/005)
- Bobra, M. G., Sun, X., Hoeksema, J. T., et al. 2014, *SoPh*, 289, 3549, doi: [10.1007/s11207-014-0529-3](https://doi.org/10.1007/s11207-014-0529-3)
- Borrero, J. M., & Ichimoto, K. 2011, *Living Reviews in Solar Physics*, 8, 4, doi: [10.12942/lrsp-2011-4](https://doi.org/10.12942/lrsp-2011-4)
- Brown, D., & Walker, A. 2021, *SoPh*, 296, 48, doi: [10.1007/s11207-021-01787-4](https://doi.org/10.1007/s11207-021-01787-4)
- Brueckner, G. E., Howard, R. A., Koomen, M. J., et al. 1995, *SoPh*, 162, 357, doi: [10.1007/BF00733434](https://doi.org/10.1007/BF00733434)
- Chen, J. 1996, *J. Geophys. Res.*, 101, 27499, doi: [10.1029/96JA02644](https://doi.org/10.1029/96JA02644)
- Chen, P. F. 2011, *Living Reviews in Solar Physics*, 8, 1, doi: [10.12942/lrsp-2011-1](https://doi.org/10.12942/lrsp-2011-1)
- Cheng, X., & Ding, M. D. 2016, *ApJS*, 225, 16, doi: [10.3847/0067-0049/225/1/16](https://doi.org/10.3847/0067-0049/225/1/16)
- Cheng, X., Ding, M. D., & Fang, C. 2015, *ApJ*, 804, 82, doi: [10.1088/0004-637X/804/2/82](https://doi.org/10.1088/0004-637X/804/2/82)
- Cheng, X., Ding, M. D., Zhang, J., et al. 2014, *ApJ*, 789, 93, doi: [10.1088/0004-637X/789/2/93](https://doi.org/10.1088/0004-637X/789/2/93)
- Cheung, M. C. M., Rempel, M., Chintzoglou, G., et al. 2019, *Nature Astronomy*, 3, 160, doi: [10.1038/s41550-018-0629-3](https://doi.org/10.1038/s41550-018-0629-3)
- Chiu, Y. T., & Hilton, H. H. 1977, *ApJ*, 212, 873, doi: [10.1086/155111](https://doi.org/10.1086/155111)
- Cirtain, J. W., Golub, L., Winebarger, A. R., et al. 2013, *Nature*, 493, 501, doi: [10.1038/nature11772](https://doi.org/10.1038/nature11772)
- Demoulin, P., Henoux, J. C., Priest, E. R., & Mandrini, C. H. 1996, *A&A*, 308, 643
- DeRosa, M. L., Wheatland, M. S., Leka, K. D., et al. 2015, *ApJ*, 811, 107, doi: [10.1088/0004-637X/811/2/107](https://doi.org/10.1088/0004-637X/811/2/107)
- DeVore, C. R. 2000, *ApJ*, 539, 944, doi: [10.1086/309274](https://doi.org/10.1086/309274)
- DeVore, C. R., & Antiochos, S. K. 2000, *ApJ*, 539, 954, doi: [10.1086/309275](https://doi.org/10.1086/309275)
- Domingo, V., Fleck, B., & Poland, A. I. 1995, *SoPh*, 162, 1, doi: [10.1007/BF00733425](https://doi.org/10.1007/BF00733425)
- Duan, A., Jiang, C., He, W., et al. 2019, *ApJ*, 884, 73, doi: [10.3847/1538-4357/ab3e33](https://doi.org/10.3847/1538-4357/ab3e33)
- Duan, A., Jiang, C., Hu, Q., et al. 2017, *ApJ*, 842, 119, doi: [10.3847/1538-4357/aa76e1](https://doi.org/10.3847/1538-4357/aa76e1)
- Duan, A., Jiang, C., Zou, P., Feng, X., & Cui, J. 2021, *ApJ*, 906, 45, doi: [10.3847/1538-4357/abc701](https://doi.org/10.3847/1538-4357/abc701)
- Dungey, J. W., & Loughhead, R. E. 1954, *Australian Journal of Physics*, 7, 5, doi: [10.1071/PH540005](https://doi.org/10.1071/PH540005)
- Fan, Y. 2009, *ApJ*, 697, 1529, doi: [10.1088/0004-637X/697/2/1529](https://doi.org/10.1088/0004-637X/697/2/1529)
- Fan, Y., & Gibson, S. E. 2007, *ApJ*, 668, 1232, doi: [10.1086/521335](https://doi.org/10.1086/521335)
- Finn, J. M., & Antonsen, Thomas M., J. 1985, *Comments on Plasma Physics and Controlled Fusion*, 9, 111
- Gary, G. A. 2001, *SoPh*, 203, 71, doi: [10.1023/A:1012722021820](https://doi.org/10.1023/A:1012722021820)
- Gilchrist, S. A., & Wheatland, M. S. 2014, *SoPh*, 289, 1153, doi: [10.1007/s11207-013-0406-5](https://doi.org/10.1007/s11207-013-0406-5)
- Gopalswamy, N., Yashiro, S., Michalek, G., et al. 2009, *Earth Moon and Planets*, 104, 295, doi: [10.1007/s11038-008-9282-7](https://doi.org/10.1007/s11038-008-9282-7)
- Grad, H., & Rubin, H. 1958, in *Proc. 2nd Int. Conf., Peaceful Uses of Atomic Energy*, 31: Theoretical and Experimental Aspects of Controlled Nuclear Fusion, ed. J. H. Martens et al. (Geneva: United Nations), 190
- Guo, J. H., Ni, Y. W., Qiu, Y., et al. 2021, *ApJ*, 917, 81, doi: [10.3847/1538-4357/ac0cef](https://doi.org/10.3847/1538-4357/ac0cef)
- Guo, Y., Cheng, X., & Ding, M. 2017a, *Science China Earth Sciences*, 60, 1408, doi: [10.1007/s11430-017-9081-x](https://doi.org/10.1007/s11430-017-9081-x)
- Guo, Y., Ding, M. D., Cheng, X., Zhao, J., & Pariat, E. 2013, *ApJ*, 779, 157, doi: [10.1088/0004-637X/779/2/157](https://doi.org/10.1088/0004-637X/779/2/157)
- Guo, Y., Ding, M. D., Schmieder, B., et al. 2010, *ApJL*, 725, L38, doi: [10.1088/2041-8205/725/1/L38](https://doi.org/10.1088/2041-8205/725/1/L38)
- Guo, Y., Xia, C., Keppens, R., & Valori, G. 2016, *ApJ*, 828, 82, doi: [10.3847/0004-637X/828/2/82](https://doi.org/10.3847/0004-637X/828/2/82)

- Guo, Y., Pariat, E., Valori, G., et al. 2017b, *ApJ*, 840, 40, doi: [10.3847/1538-4357/aa6aa8](https://doi.org/10.3847/1538-4357/aa6aa8)
- Gupta, M., Thalmann, J. K., & Veronig, A. M. 2021, *A&A*, 653, A69, doi: [10.1051/0004-6361/202140591](https://doi.org/10.1051/0004-6361/202140591)
- Harvey, J. W. 2012, *SoPh*, 280, 69, doi: [10.1007/s11207-012-0067-9](https://doi.org/10.1007/s11207-012-0067-9)
- He, W., Hu, Q., Jiang, C., Qiu, J., & Prasad, A. 2022, *ApJ*, 934, 103, doi: [10.3847/1538-4357/ac78df](https://doi.org/10.3847/1538-4357/ac78df)
- Hoeksema, J. T., Liu, Y., Hayashi, K., et al. 2014, *SoPh*, 289, 3483, doi: [10.1007/s11207-014-0516-8](https://doi.org/10.1007/s11207-014-0516-8)
- Hood, A. W., & Priest, E. R. 1979, *SoPh*, 64, 303, doi: [10.1007/BF00151441](https://doi.org/10.1007/BF00151441)
- . 1981, *Geophysical and Astrophysical Fluid Dynamics*, 17, 297, doi: [10.1080/03091928108243687](https://doi.org/10.1080/03091928108243687)
- Hu, Q., & Dasgupta, B. 2008, *SoPh*, 247, 87, doi: [10.1007/s11207-007-9090-7](https://doi.org/10.1007/s11207-007-9090-7)
- Hu, Q., Dasgupta, B., Derosa, M. L., Büchner, J., & Gary, G. A. 2010, *Journal of Atmospheric and Solar-Terrestrial Physics*, 72, 219, doi: [10.1016/j.jastp.2009.11.014](https://doi.org/10.1016/j.jastp.2009.11.014)
- Hu, Q., Qiu, J., Dasgupta, B., Khare, A., & Webb, G. M. 2014, *ApJ*, 793, 53, doi: [10.1088/0004-637X/793/1/53](https://doi.org/10.1088/0004-637X/793/1/53)
- James, A. W., Valori, G., Green, L. M., et al. 2018, *ApJL*, 855, L16, doi: [10.3847/2041-8213/aab15d](https://doi.org/10.3847/2041-8213/aab15d)
- Jiang, C., & Feng, X. 2012, *ApJ*, 749, 135, doi: [10.1088/0004-637X/749/2/135](https://doi.org/10.1088/0004-637X/749/2/135)
- . 2013, *ApJ*, 769, 144, doi: [10.1088/0004-637X/769/2/144](https://doi.org/10.1088/0004-637X/769/2/144)
- Jiang, C., Wu, S. T., Feng, X., & Hu, Q. 2014, *ApJ*, 780, 55, doi: [10.1088/0004-637X/780/1/55](https://doi.org/10.1088/0004-637X/780/1/55)
- Jiang, C., Feng, X., Liu, R., et al. 2021, *Nature Astronomy*, 5, 1126, doi: [10.1038/s41550-021-01414-z](https://doi.org/10.1038/s41550-021-01414-z)
- Jin, C. L., Harvey, J. W., & Pietarila, A. 2013, *ApJ*, 765, 79, doi: [10.1088/0004-637X/765/2/79](https://doi.org/10.1088/0004-637X/765/2/79)
- Jing, J., Park, S.-H., Liu, C., et al. 2012, *ApJL*, 752, L9, doi: [10.1088/2041-8205/752/1/L9](https://doi.org/10.1088/2041-8205/752/1/L9)
- Kilpua, E. K. J., Pomoell, J., Price, D., Sarkar, R., & Asvestari, E. 2021, *Frontiers in Astronomy and Space Sciences*, 8, 35, doi: [10.3389/fspas.2021.631582](https://doi.org/10.3389/fspas.2021.631582)
- Kliem, B., & Török, T. 2006, *PhRvL*, 96, 255002, doi: [10.1103/PhysRevLett.96.255002](https://doi.org/10.1103/PhysRevLett.96.255002)
- Lagg, A., Lites, B., Harvey, J., Gosain, S., & Centeno, R. 2017, *SSRv*, 210, 37, doi: [10.1007/s11214-015-0219-y](https://doi.org/10.1007/s11214-015-0219-y)
- Lee, H., & Magara, T. 2018, *ApJ*, 859, 132, doi: [10.3847/1538-4357/aabfe6](https://doi.org/10.3847/1538-4357/aabfe6)
- Leenaarts, J., Carlsson, M., & Rouppe van der Voort, L. 2015, *ApJ*, 802, 136, doi: [10.1088/0004-637X/802/2/136](https://doi.org/10.1088/0004-637X/802/2/136)
- Lemen, J. R., Title, A. M., Akin, D. J., et al. 2012, *SoPh*, 275, 17, doi: [10.1007/s11207-011-9776-8](https://doi.org/10.1007/s11207-011-9776-8)
- Linan, L., Pariat, É., Moraitis, K., Valori, G., & Leake, J. 2018, *ApJ*, 865, 52, doi: [10.3847/1538-4357/aadae7](https://doi.org/10.3847/1538-4357/aadae7)
- Liu, R., Kliem, B., Titov, V. S., et al. 2016, *ApJ*, 818, 148, doi: [10.3847/0004-637X/818/2/148](https://doi.org/10.3847/0004-637X/818/2/148)
- Longcope, D. W., & Malanushenko, A. 2008, *ApJ*, 674, 1130, doi: [10.1086/524011](https://doi.org/10.1086/524011)
- Low, B. C. 1985, *ApJ*, 293, 31, doi: [10.1086/163211](https://doi.org/10.1086/163211)
- . 1992, *ApJ*, 399, 300, doi: [10.1086/171925](https://doi.org/10.1086/171925)
- Mackay, D. H., Green, L. M., & van Ballegooijen, A. 2011, *ApJ*, 729, 97, doi: [10.1088/0004-637X/729/2/97](https://doi.org/10.1088/0004-637X/729/2/97)
- Maclean, R. C., Hornig, G., Priest, E. R., & Beveridge, C. 2006, *SoPh*, 235, 259, doi: [10.1007/s11207-006-0015-7](https://doi.org/10.1007/s11207-006-0015-7)
- Martínez Pillet, V., Del Toro Iniesta, J. C., Álvarez-Herrero, A., et al. 2011, *SoPh*, 268, 57, doi: [10.1007/s11207-010-9644-y](https://doi.org/10.1007/s11207-010-9644-y)
- McKenzie, D. E., & Canfield, R. C. 2008, *A&A*, 481, L65, doi: [10.1051/0004-6361:20079035](https://doi.org/10.1051/0004-6361:20079035)
- Metcalfe, T. R., De Rosa, M. L., Schrijver, C. J., et al. 2008, *SoPh*, 247, 269, doi: [10.1007/s11207-007-9110-7](https://doi.org/10.1007/s11207-007-9110-7)
- Moffatt, H. K., & Ricca, R. L. 1992, *Proceedings of the Royal Society of London Series A*, 439, 411, doi: [10.1098/rspa.1992.0159](https://doi.org/10.1098/rspa.1992.0159)
- Moraitis, K., Pariat, E., Valori, G., & Dalmasse, K. 2019a, *A&A*, 624, A51, doi: [10.1051/0004-6361/201834668](https://doi.org/10.1051/0004-6361/201834668)
- Moraitis, K., Patsourakos, S., & Nindos, A. 2021, *A&A*, 649, A107, doi: [10.1051/0004-6361/202140384](https://doi.org/10.1051/0004-6361/202140384)
- Moraitis, K., Sun, X., Pariat, É., & Linan, L. 2019b, *A&A*, 628, A50, doi: [10.1051/0004-6361/201935870](https://doi.org/10.1051/0004-6361/201935870)
- Nemenman, I. M., & Silbergleit, A. S. 1999, *Journal of Applied Physics*, 86, 614, doi: [10.1063/1.370775](https://doi.org/10.1063/1.370775)
- Pariat, E., Leake, J. E., Valori, G., et al. 2017, *A&A*, 601, A125, doi: [10.1051/0004-6361/201630043](https://doi.org/10.1051/0004-6361/201630043)
- Parker, E. N. 1983, *ApJ*, 264, 642, doi: [10.1086/160637](https://doi.org/10.1086/160637)
- . 1988, *ApJ*, 330, 474, doi: [10.1086/166485](https://doi.org/10.1086/166485)
- Pesnell, W. D., Thompson, B. J., & Chamberlin, P. C. 2012, *SoPh*, 275, 3, doi: [10.1007/s11207-011-9841-3](https://doi.org/10.1007/s11207-011-9841-3)
- Pontin, D. I., & Hornig, G. 2020, *Living Reviews in Solar Physics*, 17, 5, doi: [10.1007/s41116-020-00026-5](https://doi.org/10.1007/s41116-020-00026-5)
- Pontin, D. I., Janvier, M., Tiwari, S. K., et al. 2017, *ApJ*, 837, 108, doi: [10.3847/1538-4357/aa5ff9](https://doi.org/10.3847/1538-4357/aa5ff9)
- Priest, E. 2014, *Magnetohydrodynamics of the Sun*, doi: [10.1017/CBO9781139020732](https://doi.org/10.1017/CBO9781139020732)
- Rudenko, G. V., & Dmitrienko, I. S. 2020, *SoPh*, 295, 85, doi: [10.1007/s11207-020-01647-7](https://doi.org/10.1007/s11207-020-01647-7)
- Sadykov, V. M., & Zimovets, I. V. 2014, *Astronomy Reports*, 58, 345, doi: [10.1134/S1063772914050059](https://doi.org/10.1134/S1063772914050059)
- Sakurai, T. 1982, *SoPh*, 76, 301, doi: [10.1007/BF00170988](https://doi.org/10.1007/BF00170988)
- . 1989, *SSRv*, 51, 11, doi: [10.1007/BF00226267](https://doi.org/10.1007/BF00226267)
- Schou, J., Scherrer, P. H., Bush, R. I., et al. 2012, *SoPh*, 275, 229, doi: [10.1007/s11207-011-9842-2](https://doi.org/10.1007/s11207-011-9842-2)
- Schrijver, C. J., DeRosa, M. L., Metcalfe, T., et al. 2008, *ApJ*, 675, 1637, doi: [10.1086/527413](https://doi.org/10.1086/527413)

- Shen, J., Ji, H., & Su, Y. 2022, *Research in Astronomy and Astrophysics*, 22, 015019, doi: [10.1088/1674-4527/ac389b](https://doi.org/10.1088/1674-4527/ac389b)
- Solanki, S. K., Inhester, B., & Schüssler, M. 2006, *Reports on Progress in Physics*, 69, 563, doi: [10.1088/0034-4885/69/3/R02](https://doi.org/10.1088/0034-4885/69/3/R02)
- Solanki, S. K., Riethmüller, T. L., Barthol, P., et al. 2017, *ApJS*, 229, 2, doi: [10.3847/1538-4365/229/1/2](https://doi.org/10.3847/1538-4365/229/1/2)
- Su, Y. 2019, *ChA&A*, 43, 305, doi: [10.1016/j.chinastron.2018.09.011](https://doi.org/10.1016/j.chinastron.2018.09.011)
- Sun, X. 2013, arXiv e-prints, arXiv:1309.2392. <https://arxiv.org/abs/1309.2392>
- Sun, X., Török, T., & DeRosa, M. L. 2022, *MNRAS*, 509, 5075, doi: [10.1093/mnras/stab3249](https://doi.org/10.1093/mnras/stab3249)
- Thalmann, J. K., Gupta, M., & Veronig, A. M. 2022, *A&A*, 662, A3, doi: [10.1051/0004-6361/202243222](https://doi.org/10.1051/0004-6361/202243222)
- Thalmann, J. K., Moraitis, K., Linan, L., et al. 2019, *ApJ*, 887, 64, doi: [10.3847/1538-4357/ab4e15](https://doi.org/10.3847/1538-4357/ab4e15)
- Thalmann, J. K., Georgoulis, M. K., Liu, Y., et al. 2021, *ApJ*, 922, 41, doi: [10.3847/1538-4357/ac1f93](https://doi.org/10.3847/1538-4357/ac1f93)
- Thompson, W. T. 2006, *A&A*, 449, 791, doi: [10.1051/0004-6361:20054262](https://doi.org/10.1051/0004-6361:20054262)
- Titov, V. S., & Démoulin, P. 1999, *A&A*, 351, 707
- Titov, V. S., Hornig, G., & Démoulin, P. 2002, *Journal of Geophysical Research (Space Physics)*, 107, 1164, doi: [10.1029/2001JA000278](https://doi.org/10.1029/2001JA000278)
- Tiwari, S. K. 2012, *ApJ*, 744, 65, doi: [10.1088/0004-637X/744/1/65](https://doi.org/10.1088/0004-637X/744/1/65)
- Toriumi, S., & Park, S.-H. 2022, arXiv e-prints, arXiv:2204.06010. <https://arxiv.org/abs/2204.06010>
- Török, T., Kliem, B., & Titov, V. S. 2004, *A&A*, 413, L27, doi: [10.1051/0004-6361:20031691](https://doi.org/10.1051/0004-6361:20031691)
- Valori, G., Démoulin, P., & Pariat, E. 2012, *SoPh*, 278, 347, doi: [10.1007/s11207-012-9951-6](https://doi.org/10.1007/s11207-012-9951-6)
- Valori, G., Kliem, B., & Fuhrmann, M. 2007, *SoPh*, 245, 263, doi: [10.1007/s11207-007-9046-y](https://doi.org/10.1007/s11207-007-9046-y)
- Valori, G., Pariat, E., Anfinogentov, S., et al. 2016, *SSRv*, 201, 147, doi: [10.1007/s11214-016-0299-3](https://doi.org/10.1007/s11214-016-0299-3)
- van Ballegoijen, A. A. 2004, *ApJ*, 612, 519, doi: [10.1086/422512](https://doi.org/10.1086/422512)
- Vemareddy, P. 2019, *ApJ*, 872, 182, doi: [10.3847/1538-4357/ab0200](https://doi.org/10.3847/1538-4357/ab0200)
- Vemareddy, P., Cheng, X., & Ravindra, B. 2016, *ApJ*, 829, 24, doi: [10.3847/0004-637X/829/1/24](https://doi.org/10.3847/0004-637X/829/1/24)
- Vemareddy, P., & Zhang, J. 2014, *ApJ*, 797, 80, doi: [10.1088/0004-637X/797/2/80](https://doi.org/10.1088/0004-637X/797/2/80)
- Vissers, G. J. M., Danilovic, S., Zhu, X., et al. 2022, *A&A*, 662, A88, doi: [10.1051/0004-6361/202142087](https://doi.org/10.1051/0004-6361/202142087)
- Wang, Y., Zhuang, B., Hu, Q., et al. 2016, *Journal of Geophysical Research (Space Physics)*, 121, 9316, doi: [10.1002/2016JA023075](https://doi.org/10.1002/2016JA023075)
- Wheatland, M. S., Sturrock, P. A., & Roumeliotis, G. 2000, *ApJ*, 540, 1150, doi: [10.1086/309355](https://doi.org/10.1086/309355)
- Wiegelmann, T. 2004, *SoPh*, 219, 87, doi: [10.1023/B:SOLA.0000021799.39465.36](https://doi.org/10.1023/B:SOLA.0000021799.39465.36)
- . 2008, *Journal of Geophysical Research (Space Physics)*, 113, A03S02, doi: [10.1029/2007JA012432](https://doi.org/10.1029/2007JA012432)
- Wiegelmann, T., Inhester, B., & Sakurai, T. 2006, *SoPh*, 233, 215, doi: [10.1007/s11207-006-2092-z](https://doi.org/10.1007/s11207-006-2092-z)
- Wiegelmann, T., Petrie, G. J. D., & Riley, P. 2017, *SSRv*, 210, 249, doi: [10.1007/s11214-015-0178-3](https://doi.org/10.1007/s11214-015-0178-3)
- Wiegelmann, T., & Sakurai, T. 2021, *Living Reviews in Solar Physics*, 18, 1, doi: [10.1007/s41116-020-00027-4](https://doi.org/10.1007/s41116-020-00027-4)
- Wiegelmann, T., Thalmann, J. K., Schrijver, C. J., De Rosa, M. L., & Metcalf, T. R. 2008, *SoPh*, 247, 249, doi: [10.1007/s11207-008-9130-y](https://doi.org/10.1007/s11207-008-9130-y)
- Wiegelmann, T., Xia, L. D., & Marsch, E. 2005, *A&A*, 432, L1, doi: [10.1051/0004-6361:200500029](https://doi.org/10.1051/0004-6361:200500029)
- Yeates, A. R., & Page, M. H. 2018, *Journal of Plasma Physics*, 84, 775840602, doi: [10.1017/S0022377818001204](https://doi.org/10.1017/S0022377818001204)
- Zhang, J., Cheng, X., & Ding, M.-D. 2012, *Nature Communications*, 3, 747, doi: [10.1038/ncomms1753](https://doi.org/10.1038/ncomms1753)
- Zhang, J., Temmer, M., Gopalswamy, N., et al. 2021, *Progress in Earth and Planetary Science*, 8, 56, doi: [10.1186/s40645-021-00426-7](https://doi.org/10.1186/s40645-021-00426-7)
- Zhang, P., Chen, J., Liu, R., & Wang, C. 2022, *ApJ*, 937, 26, doi: [10.3847/1538-4357/ac8d61](https://doi.org/10.3847/1538-4357/ac8d61)
- Zhao, J., Gilchrist, S. A., Aulanier, G., et al. 2016, *ApJ*, 825, 80, doi: [10.3847/0004-637X/825/1/80](https://doi.org/10.3847/0004-637X/825/1/80)
- Zhao, J., Li, H., Pariat, E., et al. 2014, *ApJ*, 787, 88, doi: [10.1088/0004-637X/787/1/88](https://doi.org/10.1088/0004-637X/787/1/88)
- Zhao, J., Schmieder, B., Li, H., et al. 2017, *ApJ*, 836, 52, doi: [10.3847/1538-4357/836/1/52](https://doi.org/10.3847/1538-4357/836/1/52)
- Zhong, Z., Guo, Y., & Ding, M. D. 2021, *Nature Communications*, 12, 2734, doi: [10.1038/s41467-021-23037-8](https://doi.org/10.1038/s41467-021-23037-8)
- Zhou, G. P., Zhang, J., & Wang, J. X. 2016, *ApJL*, 823, L19, doi: [10.3847/2041-8205/823/1/L19](https://doi.org/10.3847/2041-8205/823/1/L19)
- Zhu, X., Neukirch, T., & Wiegelmann, T. 2022, *Sci China Tech Sci*, 65, doi: [10.1007/s11431-022-2047-8](https://doi.org/10.1007/s11431-022-2047-8)
- Zhu, X., Wang, H., Du, Z., & He, H. 2016, *ApJ*, 826, 51, doi: [10.3847/0004-637X/826/1/51](https://doi.org/10.3847/0004-637X/826/1/51)
- Zhu, X., & Wiegelmann, T. 2018, *ApJ*, 866, 130, doi: [10.3847/1538-4357/aadf7f](https://doi.org/10.3847/1538-4357/aadf7f)
- . 2019, *A&A*, 631, A162, doi: [10.1051/0004-6361/201936433](https://doi.org/10.1051/0004-6361/201936433)
- . 2022, *A&A*, 658, A37, doi: [10.1051/0004-6361/202141505](https://doi.org/10.1051/0004-6361/202141505)
- Zhu, X., Wiegelmann, T., & Inhester, B. 2020a, *A&A*, 644, A57, doi: [10.1051/0004-6361/202039079](https://doi.org/10.1051/0004-6361/202039079)

Zhu, X., Wiegmann, T., & Solanki, S. K. 2020b, *A&A*,
640, A103, doi: [10.1051/0004-6361/202037766](https://doi.org/10.1051/0004-6361/202037766)
Zou, P., Jiang, C., Wei, F., et al. 2020, *ApJ*, 890, 10,
doi: [10.3847/1538-4357/ab6aa8](https://doi.org/10.3847/1538-4357/ab6aa8)

Zuccarello, F. P., Pariat, E., Valori, G., & Linan, L. 2018,
ApJ, 863, 41, doi: [10.3847/1538-4357/aacdfc](https://doi.org/10.3847/1538-4357/aacdfc)